Author/s:
Chen, J;Pan, S;Zhou, J;Seidel, R;Beyer, S;Lin, Z;Richardson, JJ;Caruso, F

Title:
Metal–Phenolic Networks as Tunable Buffering Systems

Date:
2021

Citation:
Chen, J., Pan, S., Zhou, J., Seidel, R., Beyer, S., Lin, Z., Richardson, J. J. & Caruso, F. (2021). Metal–Phenolic Networks as Tunable Buffering Systems. Chemistry of Materials, 33 (7), pp.2557-2566. https://doi.org/10.1021/acs.chemmater.1c00015.

Metal–Phenolic Networks as Tunable Buffering Systems

Jingqu Chen,[†] Shuaijun Pan,[†] Jiajing Zhou,[†] Robert Seidel,[‡] Sebastian Beyer,[§] Zhixing Lin,[†] Joseph J. Richardson,[†] and Frank Caruso*[†]

[†]ARC Centre of Excellence in Convergent Bio-Nano Science and Technology, and the Department of Chemical Engineering, The University of Melbourne, Parkville, Victoria 3010, Australia

[‡]Helmholtz-Zentrum Berlin für Materialien and Energie. Albert-Einstein-Strasse 15, 12489 Berlin, Germany

[§]Department of Biomedical Engineering and Institute for Tissue Engineering and Regenerative Medicine (iTERM), The Chinese University of Hong Kong, Sha Tin, Hong Kong Special Administrative Region, China

ABSTRACT: The buffering effects displayed by pH-responsive polymers have recently gained attention in diverse fields such as nanomedicine and water treatment. However, creating libraries of modular and versatile polymers that can be readily integrated within existing materials remains challenging, hence restricting applications inspired by their buffering capacity. Herein, we propose the use of metal–phenolic networks (MPNs) as tunable buffering systems and through mechanistic studies show that their buffering effects are driven by pH-responsive, multivalent metal–phenolic coordination. Owing to such supramolecular interactions, MPNs exhibit ∼2-fold and 3-fold higher buffering capacity than polyelectrolyte complexes and commercial buffer solutions, respectively. We demonstrate that the MPN buffering effects are retained after deposition onto solid supports, thereby allowing stabilization of aqueous environmental pH for 1 week. Moreover, by using different metals and ligands for the films, the endosomal escape capabilities of coated nanoparticles can be tuned, where higher buffering capacity leads to greater endosomal escape. This study forms a fundamental basis for developing future metal–organic buffering materials.

INTRODUCTION

Stimuli-responsive materials undergo phase/structural transformation in response to external stimuli (e.g., temperature,[1−3] light,[4,5] solvents,[6−8] and electro/magnetic fields[9,10]). As an important subclass of stimuli-responsive materials, pH-responsive materials have been applied in diverse fields including drug delivery,[11−13] imaging,[14−16] separation processes,[17,18] surface functionalization,[19−22] and agriculture.[23,24] Generally, pH-responsive materials have acidic and/or basic moieties (e.g., carboxyl, pyridine, sulfonic, phosphate, and amine) that are susceptible to ionization (i.e., protonation or deprotonation) in response to changes in the environmental pH. The pH buffering capacity of pH-responsive materials at the nanoscale, recently termed "nanobuffering effect",[25,26] varies in magnitude depending on the buffering moieties and follows both the Henderson–Hasselbalch equation and Debye–Hückel theory.[27,28] Studies thus far have exclusively involved organic polymer systems.[29−31] However, their buffering effects and application have limitations relating to difficulties in designing and synthesizing libraries of modular and versatile polymers that can be readily integrated within existing materials. As alternatives, metal–organic hybrid systems are expected to allow for controlled buffering strengths owing to the modular and dynamic nature of the coordination bonds in such hybrid systems.[32,33] Moreover, metal–organic systems offer numerous routes for engineering pH-responsive materials.[34,35]

Metal–phenolic networks (MPNs) are a class of hybrid coordination materials that can be prepared from a wide selection of building blocks.[19] They can readily form conformal coatings on diverse templates (e.g., colloidal particles, planar/porous substrates, and microorganisms) through the dynamic coordination between phenolic ligands and metal ions.[19,36,37] Phenolic ligands that feature several phenolic groups, such as tannic acid (TA), can undergo varying degrees of (de)protonation. Therefore, MPNs can transition dynamically, crossing different coordination states. Such pH-responsive properties have been widely applied in programmable capsule degradation,[36,38−41] controlled drug delivery,[42−45] and endosomal escape.[46,47] Although the dynamic nature of the coordination bonds in MPNs is well recognized as the underlying driving force for their pH-responsiveness,[48] fundamental and systemic studies on the buffering effects that MPNs display are lacking. A key understanding of these effects at the molecular level not only will provide fundamental insights into buffering effects displayed by metal–organic systems but also will provide guidelines for developing tailorable metal–organic materials via altering building blocks for emerging applications such as intracellular pH sensors,[29] antibody purification,[25] and enzyme cascade processes.[49]

Herein, we assembled a series of MPNs in aqueous solution as nanocomplexes and as their analogues in the form of (mono-, bis-, tris-complex, aggregates, and their extended networks) continuous macroscopic thin films immobilized on substrates (including polycarbonate membranes and polystyrene nanoparticles (PS·NPs)). The coordination interactions within the MPNs (i.e., which occur at the nanoscale) allowed the exploration of the buffering mechanisms and their applications as solid-state buffers in bulk solution (i.e., macroscopic) and biological environments (i.e., microscopic), as demonstrated by the buffering of environmental pH and endosomal escape capability, respectively. As depicted in Scheme 1, the buffering effects of MPNs (in the form of both nanocomplexes and substrate-confined thin films) are driven by the pH-responsive and dynamic nature of the multivalent metal–phenolic coordination; that is, the MPNs act as a supramolecular buffer to maintain the environmental pH via altering coordination states. The MPNs displayed a stronger buffering capacity than either of the constituent building blocks (i.e., metal ions and phenolic ligands) and some commercial buffer solutions (e.g., sodium acetate (NaOAc)). In addition, careful selection of the building blocks enabled modulation of the buffering effects of the MPNs. Moreover, such buffering effects remained effective even after immobilization of the MPNs on a substrate, thereby affording MPN-coated materials as promising "solid-state buffers" capable of controlling the pH of aqueous environmental and biological systems. These findings demonstrate the potential of metal–organic hybrid materials in buffering and their subsequent applications.

RESULTS AND DISCUSSION

Different phenolic ligands (e.g., TA, gallic acid (GA), and pyrogallol (PG), Figure S1A) and metal ions (e.g., Cu^{II}, Fe^{III}, and Al^{III}; Figure S1B) were studied to examine their influence on the buffering effects of the corresponding MPNs. Firstly, titration studies were conducted to investigate the buffering capacity of TA/Fe^{III} complexes prepared by conventional coordination-driven assembly.[19] The buffering capacity (β) was calculated using the following formula:[50]

$$\beta = \frac{\Delta n}{\Delta \mathrm{pH}} \qquad (1)$$

where Δn is the change in molar concentration of hydroxide ions (OH–) with the corresponding change in pH (ΔpH). As the equivalence point on the titration curve appeared at around pH 6 for all samples examined (i.e., TA, Fe^{III}, and TA/Fe^{III} complexes (Fe^{III}:TA molar ratio of 1.5:1) (except for the blank (water) owing to its lack of buffering capacity), the buffering capacity was determined by the amount of NaOH required to reach pH 6 from the initial pH of each sample. Compared with water, TA alone exhibited slightly better buffering capacity because of its weakly acidic nature that allows proton (H^+) donation to buffer incoming OH^- (Figure 1A and 1B and Figure S2).[51] Free Fe^{III} (i.e., $FeCl_3{\cdot}6H_2O$ solution) displayed a comparable buffering capacity to TA; the buffering effect is due to the gradual displacement of the hydration layer around Fe^{III} by OH^-. The buffering effect of the Fe^{III} species is lost upon precipitation to $Fe(OH)_3$ (Figure 1A and 1B, Figure S2). In contrast, TA/Fe^{III} complexes showed the best buffering capacity to OH^- (approximately twice higher than that displayed by TA) (Figure 1A and 1B), which can be attributed to multivalent metal–phenolic coordination.[19]

The mechanism of the buffering was studied by liquid-jet X-ray photoelectron spectroscopy (XPS). The carbon 1s (C1s) electron binding energies of GA (a model phenolic ligand; Figure S3) and GA/Fe^{III} complexes in solution were examined to determine the deprotonation degrees and metal binding modes. At pH 9.5, carboxylic C1s of free GA (i.e., 1C in Figure S3) displayed a downshift of 0.81 eV compared to that of aromatic and aliphatic carboxylic acids

Scheme 1. Buffering Effects of MPNs

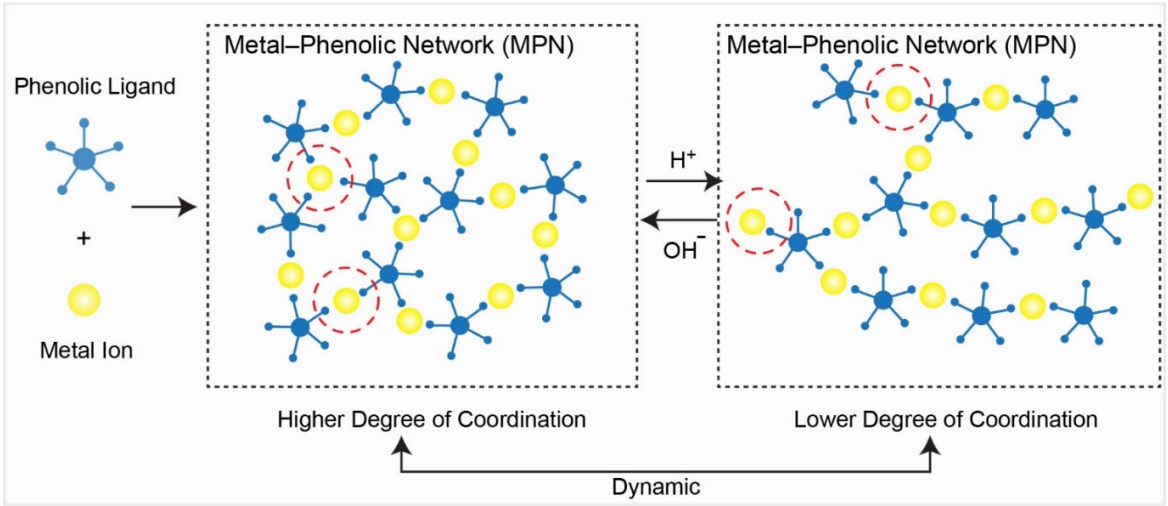

MPNs exhibit buffering effects by adjusting the degree of metal–phenolic coordination. Buffering of the incoming H^+ is achieved by pronation and switching to a lower degree of coordination (i.e., mono- and bis- dominant coordination states), whereas buffering of OH^- is achieved by deprotonation and transition to a higher degree of coordination (i.e., bis- and tris-dominant coordination states). Red circles highlight representative examples of mono, bis, and tris coordination.

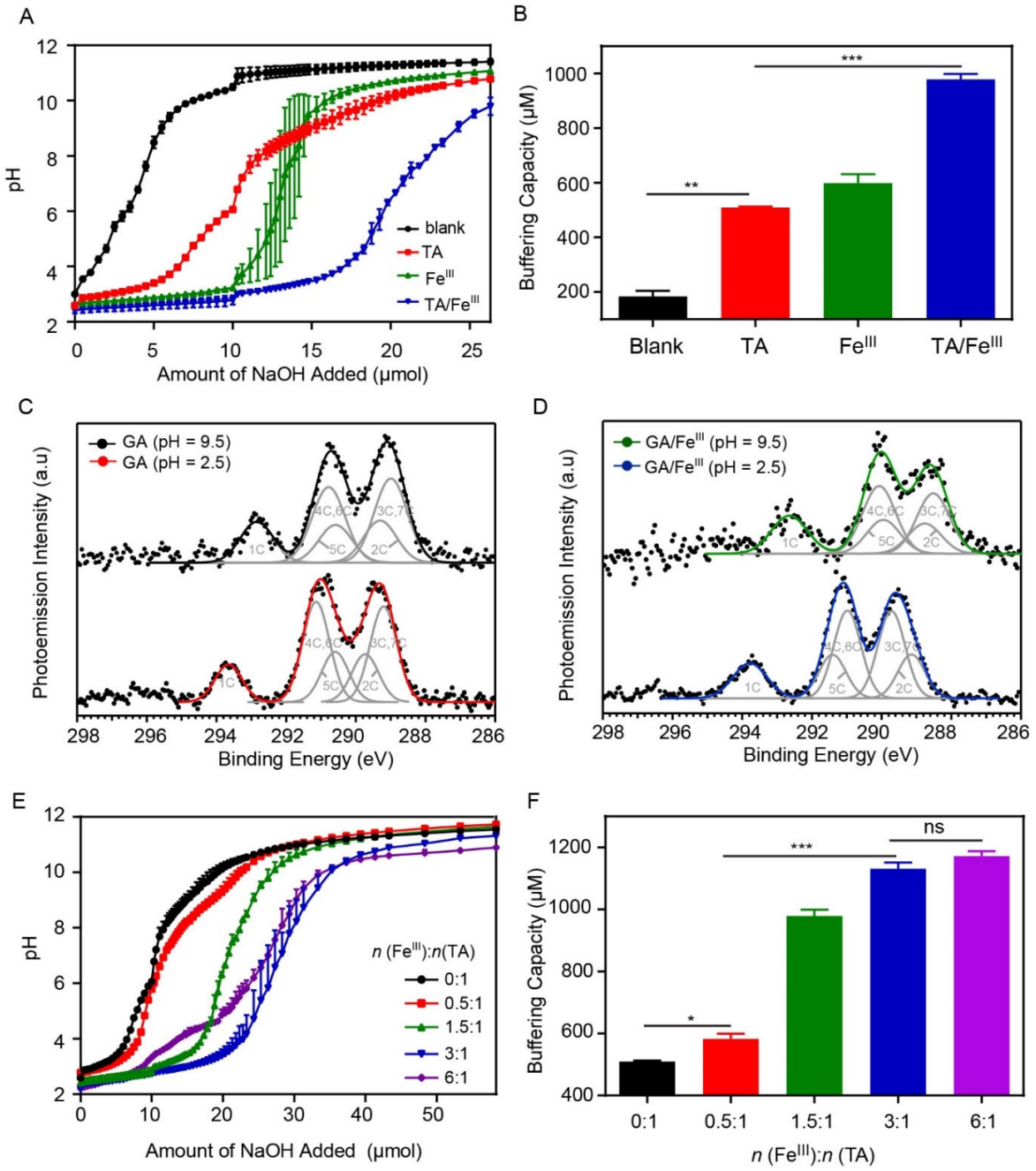

Figure 1. (A) Titration curves as a function of NaOH added and (B) buffering capacity of water (blank), TA (240 μM), $FeCl_3 \cdot 6H_2O$ (370 μM), and TA/Fe^{III} complexes (prepared from 240 μM TA and 370 μM Fe^{III} i.e., Fe^{III}:TA molar ratio of 1.5:1). $^{**}p < 0.01$ and $^{***}p < 0.001$ with 95% confidence level from unpaired *t*-test and ordinary one-way ANOVA, respectively. C1s liquid-jet XPS spectra of (C) GA and (D) GA/Fe^{III} complexes at different pH; the shifts in electron binding energy are due to deprotonation (C) and binding (D) of Fe^{III}. (E) Titration curves as a function of NaOH added and (F) buffering capacity of TA/Fe^{III} complexes prepared at different Fe^{III}:TA molar ratios (0:1, 0.5:1, 1.5:1, 3:1, and 6:1 achieved by mixing 240 μM of TA with 0, 123, 370, 740, and 1480 μM of Fe^{III}, respectively). ns, not significantly different; $^{*}p < 0.1$ with 95% confidence level from unpaired *t*-test; $^{***}p < 0.001$ with 95% confidence level from ordinary one-way ANOVA.

(~1.1 eV) reported in the literature,[52,53] as a result of GA deprotonation (Figure 1C, Table S1). Upon metal–phenolic complexation (i.e., GA/Fe^{III}), the C1s binding energies of ligand carbons (i.e., 1C–7C in Figure S3) decreased further at pH 9.5 (Figure 1C, 1D, Table S2), implying the combined effects of further deprotonation, metal–phenolic coordination, and/or carboxylic bridging. Furthermore, at pH 2.5, the GA/Fe^{III} system displayed the most significant increase of electron binding energy at 5C position (among 4C, 5C, and 6C positions) (Figure 1C, 1D, Table S3), whereas when the pH was increased to 9.5, the GA/Fe^{III} system displayed comparable binding energies across the 4C, 5C, and 6C positions (Figure 1D, Table S4). These results imply transition of the GA/Fe^{III} coordination modes/complexes,

e.g., from mono- to bis-, and/or tris-complexes.[19,54] The comparable C1s electron binding energies (~290 eV) observed among 4C, 5C, and 6C positions (Figure 1D, Table S4) also support the diverse coordination modes at pH 9.5 through 4C, 5C, and 6C between GA and Fe^{III}. Therefore, from the XPS findings and an acid–base perspective, Fe^{III}-coordination not only induces enhanced deprotonation degrees of the phenolic ligand but also enables the formation of distinct coordination modes at different pH, resulting in improved pH-buffering capacity compared with that of the ligands alone.

Increasing the Fe^{III}-to-TA (Fe^{III}:TA) molar ratio improved the buffering capacity of the TA/Fe^{III} complexes (Figure 1E, 1F). This result was supported by the reduced pKa values observed with increasing Fe^{III}:TA molar ratios (Table S5). When the Fe^{III}:TA ratio was 0.5:1, the pKa value was 3.4, which decreased to 2.6 when the ratio increased to 3:1. This trend suggests a higher the level of acidity and a higher propensity for proton donation. The higher amount of Fe^{III} might induce the generation of a larger variety of complex species in the system that are capable of buffering more OH– before reaching the tris-dominant coordination state (Figure S4). This hypothesis was supported visually by the color of the solution and UV–vis spectroscopy analyses. For example, the red tris-state was observed at pH 5 and 6 when the Fe^{III}:TA ratios were 0.5:1 and 1.5:1, respectively, whereas when the ratio increased to 3:1, the red tris-state was observed at pH 9–10 (Figure S5). As observed from Figure 1F, the buffering capacity of the TA/Fe^{III} complexes plateaued after the Fe^{III}:TA ratio reached 3:1, as most catechol groups from TA were coordinated with Fe^{III} at that ratio (i.e., further addition of Fe^{III} would not result in the generation of more complexed species) (Figure 1F). TA/Fe^{III} complexes prepared at the same Fe^{III}:TA ratio via oxidation-mediated coordination assembly[55] exhibited a similar buffering capacity, implying that the buffering capacity is related to the inherent chemical properties of the MPNs rather than their physical properties arising from the fabrication method (Figure S6).

The buffering capacity of the TA/Fe^{III} complexes was proportional to the amounts of TA and Fe^{III}, while maintaining the same Fe^{III}:TA ratio (Figure 2A). In addition,

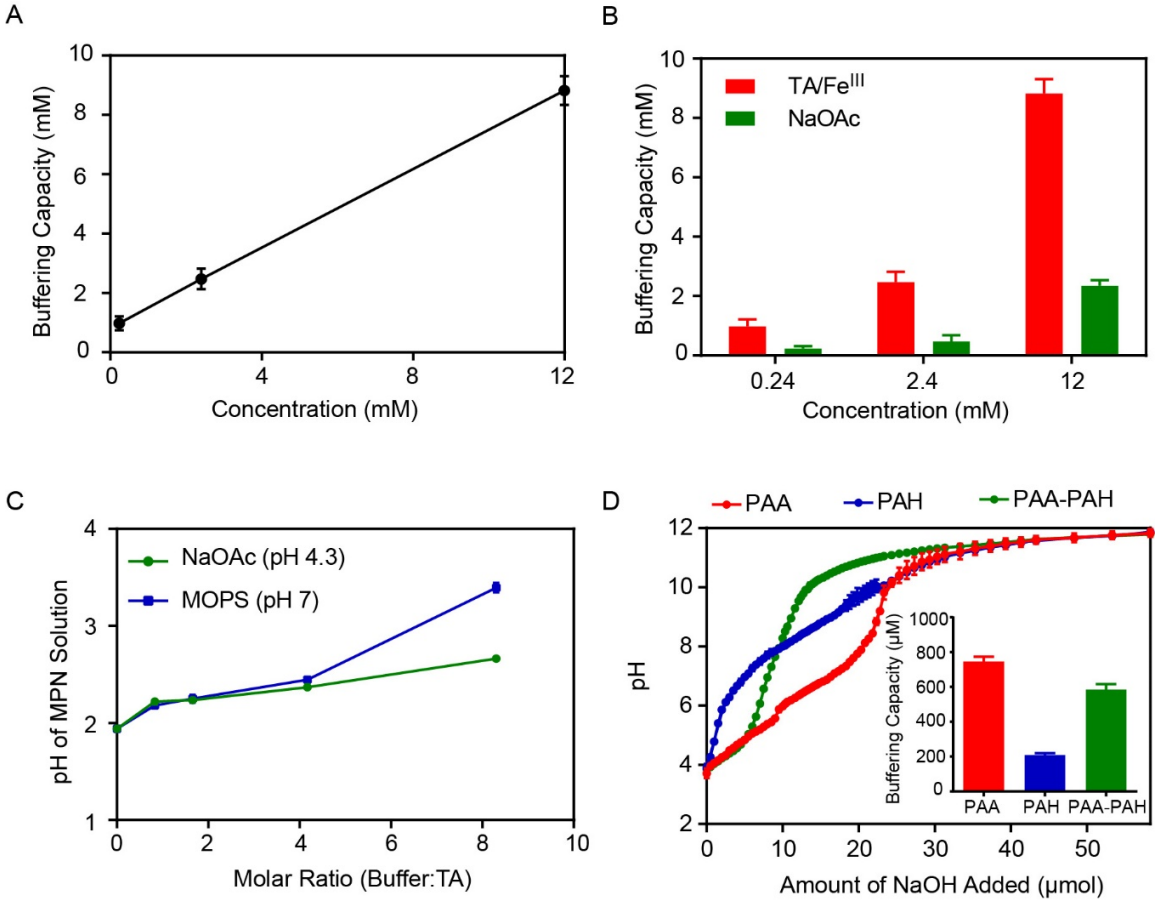

Figure 2. (A) Buffering capacity of TA/Fe^{III} complexes as a function of TA concentration while maintaining a constant Fe^{III}:TA molar ratio of 1.5:1. (B) Buffering capacities of TA/Fe^{III} complexes and commercial NaOAc at different TA concentrations. The TA concentration was varied from 0.24 to 12 mM, while maintaining a constant Fe^{III}:TA molar ratio of 1.5:1. (C) Stability of the buffering of MPNs, represented by the pH of the MPN solution (formed by mixing 1 mL of 24 mM TA and 1 mL of 37 mM Fe^{III}), upon addition of NaOAc or MOPS buffer at varying buffer-to-TA molar ratios (2 mL of 0, 10, 20, 50, and 100 mM buffer). (D) Titration curves of PAA (95 μM), PAH (37.4 μM), and PAA–PAH complex (obtained via mixing of 95 μM PAA and 37.4 μM PAH) as a function of NaOH addition and their corresponding buffering capacity profiles (inset).

as observed from Figure 2B, at the concentrations studied, TA/Fe^{III} exhibited significantly better buffering behaviors (~4-fold higher) than NaOAc, a typical buffer solution with a comparable buffering range (i.e., pH 4.0–5.5). The stability of MPN buffering effects was also explored by adding commercial buffer solutions (NaOAc and 3-(N-morpholino) propane sulfonic acid (MOPS)) to MPN solutions, followed by subsequent pH measurements. As observed in Figure 2C, TA/Fe^{III} showed an initial pH of 2, which was maintained at pH 2.5 after adding NaOAc (pH 4.3, NaOAc:TA = 8:1) and raised to pH 3.4 after adding concentrated MOPS (pH 7, MOPS:TA = 8:1). These observations demonstrate the negligible disturbance of other buffer solution on the buffering effects of MPNs.

To validate the dominant role of metal–phenolic coordination on buffering, we examined other supramolecular systems in which coordination modes are absent. Two representative polyelectrolytes (polyacrylic acid (PAA), poly(allylamine hydrochloride) (PAH)), and their supramolecular complexes (PAA–PAH) were chosen as controls. Their concentrations were adjusted so that the molar amount of their $-NH_2$ or –COOH groups matched the molar amount of the phenolic groups of TA (30 μmol). PAA and PAH are both widely used to assemble layer-by-layer thin films through electrostatic interactions and hydrogen bonding.[56,57] Relative to PAA, PAA–PAH complexion resulted in a reduction of 24% in the buffering capacity (Figure 2D), implying that the synergistic buffering effects displayed by TA/Fe^{III} complexes were due to the dynamic metal–phenolic coordination that can transition between different coordination states in the MPN system.

To further examine the stability of the buffering capacity of MPNs when deposited onto substrates, TA/Fe^{III}-coated polycarbonate membranes were engineered into solid-state buffers to mitigate acidification of aqueous solutions. The solid-state buffers were obtained by coating polycarbonate membranes with TA/Fe^{III} and subsequently increasing the pH to promote the coordination between TA and Fe^{III} in bis- and tris- dominant states. As observed from Figure 3A and 3B, the pH of water treated with the solid-state MPN buffer remained relatively constant at ~7, whereas that of pure water and water treated with an uncoated membrane decreased from 7.5 to ~5 after 1 week. A decrease in the pH of water is typically observed because of the increased level of dissolved carbon dioxide upon contact with the atmosphere. Following the incubation test of the solid-state buffer, the TA/Fe^{III} complexes remained mainly on the substrate (e.g., polycarbonate membrane and glass slide), as confirmed by the preservation of a ligand-to-metal charge transfer band between 500 and 600 nm in the UV–vis spectrum of the coated glass slide along with the consistent surface properties and elemental compositions displayed by the coated membranes before and after the incubation test, while the released TA might be from unbound TA molecules (Figures 3C, S7, and S8).In addition, the solid-state MPN buffer could reduce the acidity of dilute hydrochloride acid (1 mM HCl) and raise the pH from 3.6 to 5.1 (Figure S9), with the magnitude of pH modulation controlled by the number of MPN layers deposited on the membrane.

Owing to the vast library of building blocks from which MPNs can be assembled, the ligand and metal dependence of the buffering of MPNs were examined. To explore the effect of phenolic ligands with different functional groups, GA/Fe^{III}, PG/Fe^{III}, and TA/Fe^{III} complexes were prepared with the same molar ratio of phenolic groups. PG/Fe^{III} and TA/Fe^{III} displayed similar buffering capacity (Figure 4A) because of the same functional chemical moieties (i.e., –OH) present in these complexes (Figure S1A). In contrast, GA/Fe^{III} complexes exhibited a higher buffering capacity (1.6-fold; Figures 4A and S10A) despite having a comparable experimental pK_a value to those of PG/Fe^{III} and TA/Fe^{III} complexes (Table S6). This higher buffering capacity could be attributed to the carboxylic acid groups of GA that can provide additional binding sites for the Fe^{III} species (Figure S10B).[58] The different buffering capacities displayed by GA/Fe^{III} and TA/Fe^{III} complexes were also reflected by the color of the respective complex solutions.

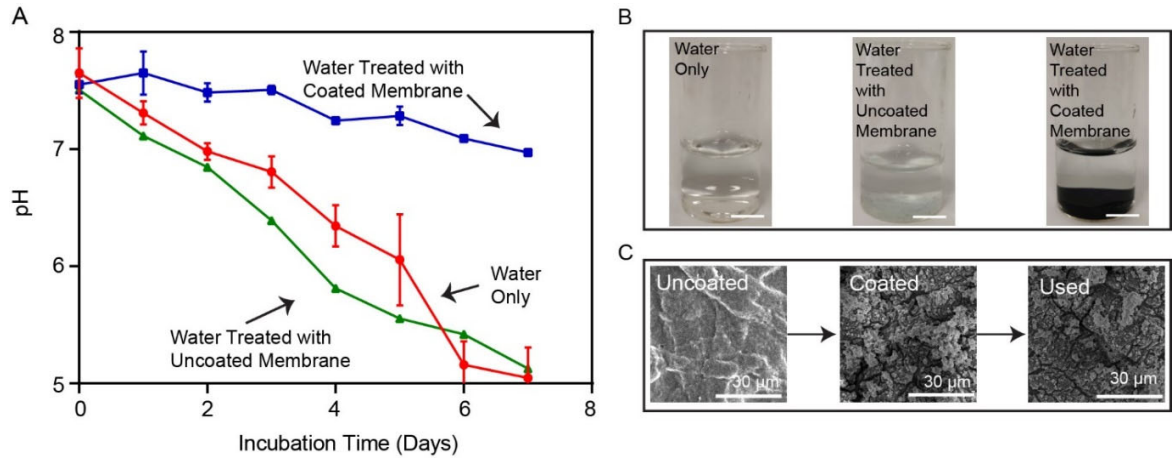

Figure 3. (A) pH of water (5 mL) as a function of incubation time (days): water treated with a TA/Fe^{III}-coated membrane or an uncoated membrane or without a membrane. (B) Photographs of the corresponding water solutions subjected to the different treatments. Scale bars are 2 cm. (C) Scanning electron microscopy images of the uncoated, TA/Fe^{III}-coated, and used membranes.

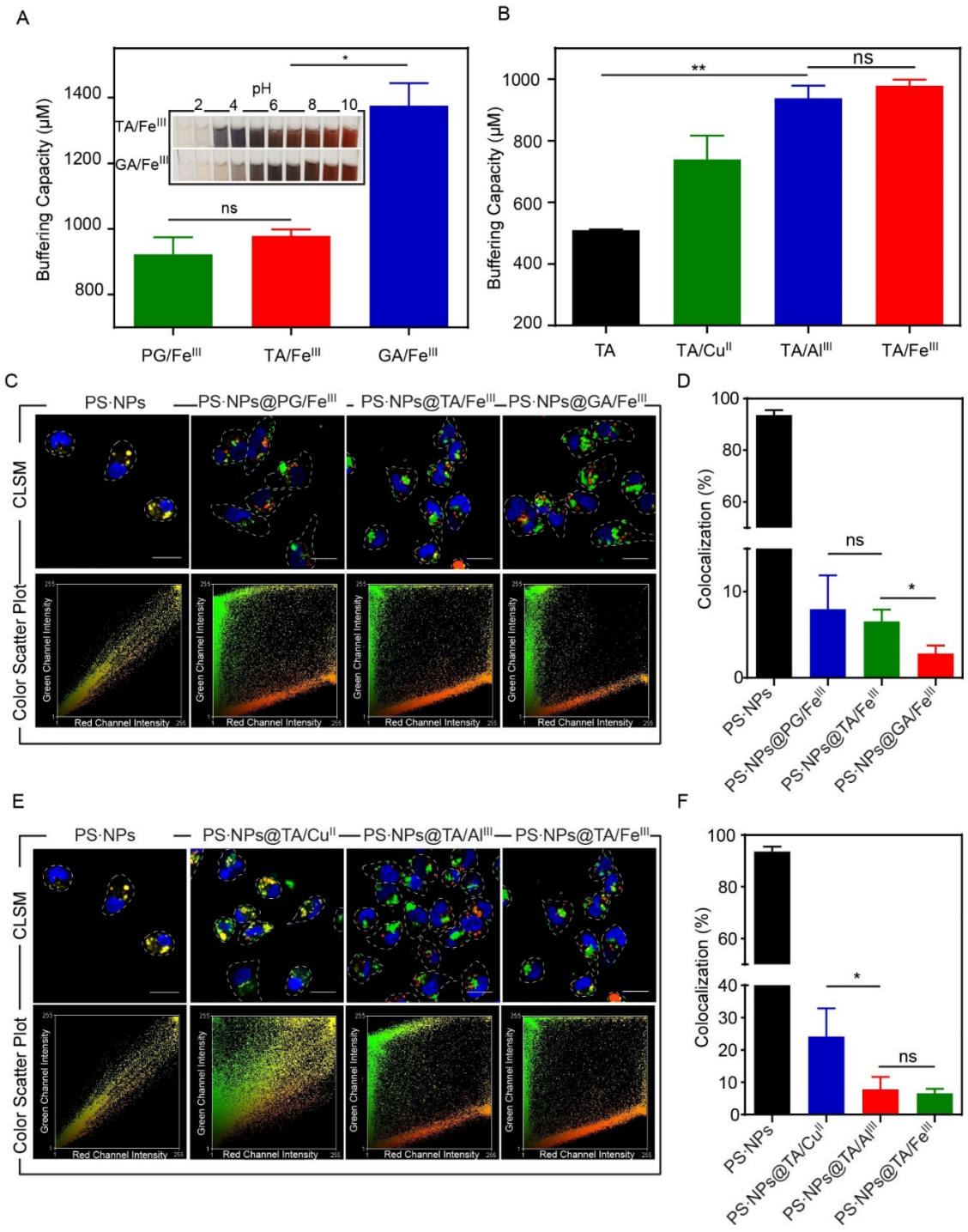

Figure 4. Buffering capacity of (A) Fe^{III}-based MPNs formed by complexing Fe^{III} with different phenolic ligands. The concentrations of Fe^{III}, PG, GA, and TA are 370, 2400, 2400, and 240 μM, respectively. Insets are photographs of the solutions of the Fe^{III}-based MPNs with different phenolic ligands displaying pH-dependent color patterns. (B) Buffering capacities of TA and TA-based MPNs formed by complexing TA with different metals. The concentrations of TA and the metal ions were 240 and 370 μM, respectively. Representative confocal laser scanning microscopy (CLSM) images and corresponding color scatter plots of MDA-MB-231 cells incubated with pristine PS·NPs or PS·NPs coated with (C) Fe^{III}-based MPNs with different phenolic ligands or (E) TA-based MPNs with different metal ions for 4 h at a particle-to-cell ratio of 3000:1. NPs (green) were fluorescently labeled. Endo/lysosomes (red) were stained with LysoTracker Red. Nuclei (blue) were stained with Hoechst 33342. The dashed lines in the merged CLSM images indicate the cellular boundaries based on the corresponding bright-field images (Figure S14). Scale bars are 20 μm. Percentage of colocalization with endo/lysosomes of pristine PS·NPs and PS·NPs coated with (D) Fe^{III}-based MPNs with different phenolic ligands or (F) TA-based MPNs with different metal ions. ns, not significantly different; *p < 0.1 with 95% confidence level from unpaired t-test; **p < 0.01 with 95% confidence level from ordinary one-way ANOVA.

The red tris- dominant state was observed at around pH 6 for TA/Fe^{III} complexes and at pH 8–9 for GA/Fe^{III} complexes (Figure 4A insets).

The effect of metals on the buffering capacity of MPN complexes was investigated by complexing TA with different metals (Cu^{II}, Al^{III}, or Fe^{III}). A metal-to-TA molar ratio of 1.5:1 was selected because of the higher coating compatibility (i.e., without precipitation/aggregation; Figure S5A) achieved with all examined metals at that ratio when compared with other ratios. As illustrated in Figures 4B and S11A, the buffering capacity decreased in the order of TA/Fe^{III} ≈ TA/Al^{III} >> TA/Cu^{II} > TA. This trend suggests that metals with higher coordination coefficients are likely to coordinate with a greater amount of catechol groups stoichiometrically and form tris-complexes, allowing for more diverse coordination states to exist in the MPN system (Figure S11B, Table S7).

The ability to control the buffering of MPNs through the choice of specific metals and ligands could allow for the engineering of target environmental responses, e.g., tunable endosomal escape behavior. Endosomal escape has been regarded as a key bottleneck for cytosolic delivery of therapeutic cargos.[46] Controlling endosomal escape offers opportunities for safe and effective intracellular delivery, and potentially optimal therapeutic outcomes.[59] Therefore, we further examined different MPN systems (different ligands and metals) to determine whether their nanobuffering potential influences their endosomal escape properties. The colocalization of MPN-coated PS·NPs (PS·NPs@MPNs) with endo/lysosomes was evaluated where the PS·NPs were labeled with green fluorescence and the endo/lysosomes were stained with LysoTracker Red. Pristine PS·NPs could not escape from endo/lysosomes, as indicated by the large proportion of yellow region under CLSM (nearly ~100% of colocalization). In contrast, coating of the PS·NPs with PG/Fe^{III}, TA/Fe^{III}, or GA/Fe^{III} enabled endosomal escape without altering the cell viability, as indicated by the separate green and red regions in the CLSM images and a significantly lower percentage of colocalization (<10%; Figures 4C, 4D, and S12A, S13). Among the MPN-coated PS·NPs, PS·NPs@GA/Fe^{III} showed the lowest percentage of colocalization with endo/lysosomes (~3%) (Figure 4D), suggesting the highest endosomal escape ability correlates with the highest buffering capacity (Figure 4A). The negligible difference in the percentage of colocalization between PS·NPs@TA/Fe^{III} and PS·NPs@PG/Fe^{III} (~7% and ~8%, respectively) is also consistent with the negligible difference in buffering effects displayed by the two systems (Figure 4A). Comparison of the PS·NPs coated with MPNs of different metal ions revealed the same trend as the MPNs composed of different ligands, namely that higher buffering capacity correlated with greater endosomal escape. Specifically, PS·NPs@TA/Cu^{II} had significantly higher co-localization (i.e., a lower degree of escape) than PS·NPs@TA/Fe^{III} or PS·NPs@TA/Al^{III} (~27% vs <10%; Figure 4E, 4F, and S12B). Collectively, these results demonstrate that the buffering effects of MPNs can be tailored through the choice of the building blocks and that this control can influence their endosomal escape properties.

CONCLUSION

We explored the fundamental chemistry underlying the buffering effects of MPNs. This allowed us to examine how the building block choice influences buffering in metal–organic systems, where we observed that stronger chelating metals, and ligands with higher binding strengths both increase the buffering capacity. Specifically, the synergistic effects from pH-responsive multivalent metal–phenolic coordination endowed the MPNs with significantly better buffering capacity than the corresponding building blocks, that is, the ligands and metal ions. Altering the building blocks of the MPNs afforded modular control over the buffering of MPNs by adjusting the degree of metal–phenolic coordination and of the different coordination modes for multistage transitions. Moreover, the buffering effects of the MPN complexes were preserved after their immobilization on solid surfaces, and pH modulation in both simple and complex aqueous conditions could still be achieved. For example, we demonstrated that the buffering capacity of different MPNs can modulate the endosomal escape properties of coated nanoparticles, where stronger buffering materials yielded higher endosomal escape. This study also provides fundamental insights into metal–organic systems and will facilitate the design of materials capable of controlling the pH in various environments ranging from intracellular compartments to water bodies.

EXPERIMENTAL SECTION

Materials. TA, GA, PG, $FeCl_3·6H_2O$, $FeCl_2·4H_2O$, $AlCl_3·6H_2O$, $CuCl_2·4H_2O$, NaOAc, NaOH, Dulbecco's phosphate-buffered saline (DPBS), MOPS, phenazine methosulfate, PAA (M_w = 6000), and PAH (M_w = 15 000) were purchased from Sigma-Aldrich (USA). Polycarbonate membranes with pore sizes of ~0.4 μm were purchased from Merck. Dulbecco's modified Eagle's medium (DMEM), LysoTracker Red DND-99, 2,3-bis[2-methoxy-4-nitro-5-sulfophenyl]-2*H*-tetrazolium-5-carboxyanilide inner salt, and trihydrochloride (Hoechst 33342, 10 mg mL^{-1}) were obtained from Life Technologies. Green fluorescent PS·NPs (285 ± 8 nm, 2.5% w/v) were purchased from microParticles (GmbH). All chemicals were used as received without further purification. The pH values of the solutions were measured with a Mettler-Toledo MP220 pH meter. Milli-Q water with a resistivity greater than 18.2 MΩ cm was obtained from a three-stage Millipore Milli-Q plus 185 purification system (Millipore Corporation, USA). All aqueous solutions were filtered with 220 nm diameter membranes before the cell experiments.

Buffering Capacity of TA/Fe^{III} Complexes Obtained from Discrete Assembly. The buffering capacity of TA/Fe^{III} complexes, obtained by discrete assembly, was evaluated by titration. TA (50 μL, 24 mM) and 50 μL of $FeCl_3·6H_2O$ (37 mM) were successively added to 4.9 mL of Milli-Q water (corresponding to an Fe^{III}-to-TA molar ratio *n* (Fe^{III}):*n* (TA) = 1.5:1), followed by stirring for 1 min Then, 0.1 M NaOH was added dropwise to the suspension under stirring, and the corresponding pH was measured. To achieve different Fe^{III}:TA molar ratios (i.e., 0.5:1, 3:1, and 6:1), the amount of TA remained the same while the concentration of $FeCl_3·6H_2O$ was adjusted to 12.3, 74, and 148 mM, respectively. The following solutions were used as controls: 5 mL of Milli-Q water, 50 μL of TA (24 mM) in 4.95 mL of Milli-Q water, and 50 μL of $FeCl_3·6H_2O$ (37 mM) in 4.95 mL of Milli-Q water. The buffering capacity was calculated using

Equation 1. To estimate the pK_a values of the MPN complexes, the equivalence point was first identified. The pH corresponding to the half-equivalence point was estimated as the pK_a.

Preparation of TA/Fe^{III} Coatings on Polycarbonate Membranes. Polycarbonate membranes were immersed in 3 mL of TA (4.8 mM) solution, followed by addition of 3 mL of $FeCl_2 \cdot 4H_2O$ (48 mM) solution. The mixed solution was shaken at 80 rpm on a platform mixer for 20 h. The pH was then increased by adding 1 mL of NaOH (0.1 M). The obtained TA/Fe^{III}-coated membranes were thoroughly rinsed by Milli-Q water and dried under a stream of air.

Liquid-Jet XPS Measurements. The C1s photoelectron spectra were recorded using the SOL^{3}PES experimental setup at the U49/2-PGM-1 beamline at the synchrotron radiation facility BESSY II in Berlin, Germany.[60] The detection of the photoelectrons was carried out in magic-angle geometry, i.e. the angle between the polarization vector of the X-ray beam and the Scienta Omicron R4000 HiPP-2 hemispherical electron analyzer was 54.7°. In this geometry, photoelectron angular distribution effects are negligible, and differential ionization cross-sections are directly proportional to the total ionization cross-section, allowing comparison of the peak areas of different C1s photoelectron peaks. The liquid jet was produced by injecting the aqueous GA solutions through a nozzle of fused silica with an inner diameter of 25 μm. A flow rate of 1 mL min^{-1} was maintained at a pressure of approximately 4 bar using a high-performance liquid-chromatography pump (Techlab Model Economy). The temperature of the solutions prior to injection was 20 °C, which was controlled and set by a refrigerated/heating circulator (Julabo F12/ED). The interaction with the X-rays occurred approximately 0.5 mm from the top of the glass capillary. At that location, the liquid jet follows the laminar flow regime. Further downstream (~1 cm, depending on the nozzle diameter, flow rate, and liquid), the flow turns turbulent, and finally at several centimeters downstream, the jet breaks into droplets. These droplets are caught by a cold trap, a metal cylinder filled with liquid nitrogen, minimizing the gas load from the evaporating liquid. During measurements, the pressure inside the vacuum chamber was ~8×10^{-4} mbar, which was maintained using a turbomolecular pump (Pfeiffer 1600 L s^{-1}) and one additional liquid-nitrogen cold trap.

The energy resolution of the U49/2-PGM-1 beamline was better than 260 meV at 850 eV photon energy used for the C1s measurements. Together with the resolution of the electron analyzer of 450 meV at 200 eV pass energy, the total energy resolution in our experiment was approximately 520 meV. The focal size of the X-ray beam was 80×50 μm^2, in the same order of magnitude than the liquid jet diameter. The distance between the interaction point and the electron analyzer entrance (an orifice of 500 μm in diameter) was approximately 500 μm. This short distance ensures that the emitted photoelectrons reach the entrance without significantly interacting/scattering with the surrounding gas sheet of the jet. Further details on the SOL^{3}PES setup and the liquid jet method can be found elsewhere.[61,62]

Characterization. The surface of the membranes with and without MPN coatings and their elemental composition were characterized by scanning electron microscopy and energy-dispersive X-ray spectroscopy mapping. UV–vis absorption measurements were carried out on a Varian Cary 4000 UV–vis spectrophotometer.

Cell Culture. Human breast adenocarcinoma cell line (MDA-MB-231) was purchased from the American Type Culture Collection. MDA-MB-231 cells with a low passage number (between 27 and 50) were cultured in complete DMEM supplied with 10% fetal bovine serum (FBS) at 37 °C, 5% CO_2, and 95% humidity.

MPN Coating on NP Templates for Colocalization Studies. All aqueous solutions were prepared freshly prior to use. Before coating, 50 μL of green fluorescent PS·NPs suspension was washed twice with Milli-Q water via centrifugation (10 000 *g*, 10 min) and subsequently dispersed in 440 μL of Milli-Q water. To prepare TA-based MPN coatings with different metals, 5 μL of $FeCl_3 \cdot 6H_2O$, $AlCl_3 \cdot 6H_2O$, or $CuCl_2 \cdot 4H_2O$ (37 mM) and 5 μL of TA (24 mM) were successively added to the suspension followed by brief vortexing and sonication after each addition to avoid aggregation. The pH of the suspension during assembly was controlled to 5 by adding 500 μL of NaOAc (100 mM). The mixed suspension was vortexed for 1 min and allowed to sit undisturbed for 5 min to achieve sufficient film formation and adherence. The coated NP suspension was then washed three times with 1 mL of Milli-Q water (10 000 *g*, 10 min) and finally dispersed in 500 μL of DPBS for subsequent cell experiments. Fe^{III}-based MPN coatings with different phenolic ligands were prepared by using the same protocol except that the following precursor solutions were used instead—50 μL of $FeCl_3 \cdot 6H_2O$ (37 mM) and 5 μL of PG (240 mM), or 50 μL of GA (24 mM). These amounts were chosen so that these ligands have the same number of moles of the phenolic groups.

Colocalization by CLSM. MDA-MB-231 cells were seeded in an 8-well Lab-Tek-Chamber slide at a density of 30 000 cells per well in 400 μL of DMEM supplied with 10% FBS for 20 h. After incubation, the culture media was removed and replaced with 200 μL of fresh media to reduce the sedimentation distance for NPs. Then, a series of PS·NPs@MPNs were added to the cells at a density of 3000:1 (NP-to-cell ratio) and incubated for 4 h. To investigate the endosomal escape of the NPs, the cell sample was gently washed twice with 400 μL of DPBS to remove excess NPs, and the endo/lysosomal compartment was stained with LysoTracker Red (final concentration of 100 nM in the complete cell media) for 1 h following the supplier's protocol. After incubation, cells were gently washed three times with DPBS and incubated with Hoechst 33342 (1 μg mL^{-1}) for 10 min to stain the nucleus. Then, the cells were live-imaged using a Nikon A1R confocal microscope with a 40× water immersion objective. To quantify the correlation between green and red fluorescence signals, Pearson's correlation coefficient (PCC) values and color scatter plots were obtained using the WCIF ImageJ software. To quantify the percentage of colocalization, WCIF ImageJ software was used to identify the colocalized regions (i.e., regions of yellow). Then, the ratio of the area of the yellow regions to the total area of

green and yellow regions was calculated as the percentage of colocalization. Five representative cell images (cell count ≥50) were used to calculate the PCC values and the percentage of colocalization, and the results are presented as means ± standard deviations. When the cell count increased to 100, the colocalization percentage was 9 ± 3%, which is not statistically different from the colocalization percentage obtained with a lower cell count (≥50).

ASSOCIATED CONTENT

Supporting Information. Experimental details, molecular structures of phenolic ligands and hydrated metal ions, UV–vis spectra, energy-dispersive X-ray spectroscopy mapping images, CLSM images with bright-field references, Pearson's correlation coefficient values, titration curves, experimental pK_a values, C1s electron binding energy values, and MIRIBEL checklist for reporting research in bio–nano science.[63] This material is available free of charge via the Internet at http://pubs.acs.org.

AUTHOR INFORMATION

Corresponding Author

* E-mail: fcaruso@unimelb.edu.au.

Author Contributions

The manuscript was written through the contribution of all authors. All authors have given approval to the final version of the manuscript.

Notes

The authors declare no competing financial interest.

ACKNOWLEDGMENT

This research was conducted and funded by the Australian Research Council Centre of Excellence in Convergent Bio-Nano Science and Technology (project number CE140100036). F.C. acknowledges the award of a National Health and Medical Research Council Senior Principal Research Fellowship (GNT1135806). This work was performed in part at the Materials Characterisation and Fabrication Platform (MCFP) at The University of Melbourne and the Victorian Node of the Australian National Fabrication Facility (ANFF). R.S. acknowledges the German Research Foundation (DFG) for an Emmy-Noether grant (SE 2253/3-1). S.B. acknowledges the award of grant 4055120 from The Chinese University of Hong Kong. The authors appreciate support from the HelmholtzZentrum Berlin for granting beamtime (no. 191-07915-ST) at the U49/2-PGM-1 undulator beamline with the SOL^{3}PES setup at BESSY II and experimental support from Dominik Al-Sabbagh from the Federal Institute for Materials Research and Testing (BAM).

REFERENCES

(1) Yang, Y.; Zhu, W.; Dong, Z.; Chao, Y.; Xu, L.; Chen, M.; Liu, Z. 1D Coordination Polymer Nanofibers for Low-Temperature Photothermal Therapy. *Adv. Mater.* **2017**, *29*, 1703588.
(2) Cui, Y.; Wang, Y.; Shao, Z.; Mao, A.; Gao, W.; Bai, H. Smart Sponge for Fast Liquid Absorption and Thermal Responsive Self-Squeezing. *Adv. Mater.* **2020**, *32*, e1908249.
(3) Sun, M. J.; Zhong, Y. W.; Yao, J. Thermal-Responsive Phosphorescent Nanoamplifiers Assembled from Two Metallophosphors. *Angew. Chem. Int. Ed.* **2018**, *57*, 7820–7825.
(4) Zhang, Y. M.; Liu, Y. H.; Liu, Y. Cyclodextrin-Based Multistimuli-Responsive Supramolecular Assemblies and Their Biological Functions. *Adv. Mater.* **2020**, *32*, e1806158.
(5) Smit, B.; Huwe, F.; Payne, N.; Olaoye, O.; Bauer, I.; Pflaum, J.; Schwoerer, M.; Schwoerer, H. Ultrafast Pathways of the Photoinduced Insulator–Metal Transition in a Low-Dimensional Organic Conductor. *Adv. Mater.* **2019**, *31*, e1900652.
(6) Hillerström, A.; Andersson, M.; Samuelsson, J.; van Stam, J. Solvent Strategies for Loading and Release in Mesoporous Silica. *Colloid Interface Sci. Commun.* **2014**, *3*, *5–8*.
(7) Hoelzel, C. A.; Hu, H.; Wolstenholme, C. H.; Karim, B. A.; Munson, K. T.; Jung, K. H.; Zhang, H.; Liu, Y.; Yennawar, H. P.; Asbury, J. B.; Li, X.; Zhang, X. A General Strategy to Enhance Donor-Acceptor Molecules Using Solvent-Excluding Substituents. *Angew. Chem. Int. Ed.* **2020**, *59*, 4785–4792.
(8) Matsumoto, K.; Kusaba, S.; Tanaka, Y.; Sei, Y.; Akita, M.; Aritani, K.; Haga, M. A.; Yoshizawa, M. A Peanut-Shaped Polyaromatic Capsule: Solvent-Dependent Transformation and Electronic Properties of a Non-Contacted Fullerene Dimer. *Angew. Chem. Int. Ed.* **2019**, *58*, 8463–8467.
(9) Chen, W.; Cheng, C. A.; Zink, J. I. Spatial, Temporal, and Dose Control of Drug Delivery Using Non-Invasive Magnetic Stimulation. *ACS Nano* **2019**, *13*, 1292–1308.
(10) Xu, X.; Hou, S.; Wattanatorn, N.; Wang, F.; Yang, Q.; Zhao, C.; Yu, X.; Tseng, H. R.; Jonas, S. J.; Weiss, P. S. Precision-Guided Nanospears for Targeted and High-Throughput Intracellular Gene Delivery. *ACS Nano* **2018**, *12*, 4503–4511.
(11) Ulrich, S. Growing Prospects of Dynamic Covalent Chemistry in Delivery Applications. *Acc. Chem. Res.* **2019**, *52*, 510–519.
(12) Viricel, W.; Mbarek, A.; Leblond, J. Switchable Lipids: Conformational Change for Fast pH-Triggered Cytoplasmic Delivery. *Angew. Chem. Int. Ed.* **2015**, *54*, 12743–12747.
(13) Ping, Y.; Ding, D.; Ramos, R.; Mohanram, H.; Deepankumar, K.; Gao, J.; Tang, G.; Miserez, A. Supramolecular β-Sheets Stabilized Protein Nanocarriers for Drug Delivery and Gene Transfection. *ACS Nano* **2017**, *11*, 4528–4541.
(14) Xiong, H.; Zuo, H.; Yan, Y.; Occhialini, G.; Zhou, K.; Wan, Y.; Siegwart, D. J. High-Contrast Fluorescence Detection of Metastatic Breast Cancer Including Bone and Liver Micrometastases via Size-Controlled pH-Activatable Water-Soluble Probes. *Adv. Mater.* **2017**, *29*, 1700131.
(15) Zhang, H.; Hao, C.; Qu, A.; Sun, M.; Xu, L.; Xu, C.; Kuang, H. Heterostructures of MOFs and Nanorods for Multimodal Imaging. *Adv. Funct. Mater.* **2018**, *28*, 1805320.
(16) Weng, G.; Thanneeru, S.; He, J. Dynamic Coordination of Eu-Iminodiacetate to Control Fluorochromic Response of Polymer Hydrogels to Multistimuli. *Adv. Mater.* **2018**, *30*, 1706526.
(17) Song, Y.; Fan, J. B.; Li, X.; Liang, X.; Wang, S. pH-Regulated Heterostructure Porous Particles Enable Similarly Sized Protein Separation. *Adv. Mater.* **2019**, *31*, e1900391.
(18) Liu, H.; Zhu, J.; Hao, L.; Jiang, Y.; van der Bruggen, B.; Sotto, A.; Gao, C.; Shen, J. Thermo- and pH-Responsive Graphene Oxide Membranes with Tunable Nanochannels for Water Gating and Permeability of Small Molecules. *J. Membr. Sci.* **2019**, *587*, 117163.
(19) Ejima, H.; Richardson, J. J.; Liang, K.; Best, J. P.; Koeverden, M.; Such, G. K.; Cui, J.; Caruso, F. One-Step Assembly of Coordination Complexes for Versatile Film and Particle Engineering. *Science* **2013**, *341*, 154–157.
(20) Li, J.; Angsantikul, P.; Liu, W.; Esteban-Fernandez de Avila, B.; Thamphiwatana, S.; Xu, M.; Sandraz, E.; Wang, X.; Delezuk, J.; Gao, W.; Zhang, L.; Wang, J. Micromotors Spontaneously Neutralize Gastric Acid for pH-Responsive Payload Release. *Angew. Chem. Int. Ed.* **2017**, *56*, 2156–2161.
(21) Yang, G.; Xu, L.; Xu, J.; Zhang, R.; Song, G.; Chao, Y.; Feng, L.; Han, F.; Dong, Z.; Li, B.; Liu, Z. Smart Nanoreactors for pH-Responsive Tumor Homing, Mitochondria-Targeting, and Enhanced

Photodynamic-Immunotherapy of Cancer. *Nano Lett.* **2018**, *18*, 2475–2484.
(22) Zhou, X.; He, C. Tailoring the Surface Chemistry and Morphology of Glass Fiber Membranes for Robust Oil/Water Separation Using Poly(dimethylsiloxanes) as Hydrophobic Molecular Binders. *J. Mater. Chem. A* **2018**, *6*, 607–615.
(23) Hill, M. R.; MacKrell, E. J.; Forsthoefel, C. P.; Jensen, S. P.; Chen, M.; Moore, G. A.; He, Z. L.; Sumerlin, B. S. Biodegradable and pH-Responsive Nanoparticles Designed for Site-Specific Delivery in Agriculture. *Biomacromolecules* **2015**, *16*, 1276–1282.
(24) Ning, Q.; Chen, L.; Jia, Z.; Zhang, C.; Ma, D.; Li, F.; Zhang, J.; Li, D.; Han, X.; Cai, Z.; Huang, S.; Liu, W.; Zhu, B.; Li, Y. Multiple Long-Term Observations Reveal a Strategy for Soil pH-Dependent Fertilization and Fungal Communities in Support of Agricultural Production. *Agric., Ecosyst. Environ.* **2020**, *293*, 106837.
(25) Palapuravan, A.; Zhao, Y.; Greschner, A. A.; Congdon, T. R.; de Haan, H. W.; Cottenye, N.; Gauthier, M. A. Evidence, Manipulation, and Termination of pH "Nanobuffering" for Quantitative Homogenous Scavenging of Monoclonal Antibodies. *ACS Nano* **2019**, *13*, 1019–1028.
(26) Tao, W.; Wang, J.; Parak, W. J.; Farokhzad, O. C.; Shi, J. Nanobuffering of pH-Responsive Polymers: A Known but Sometimes Overlooked Phenomenon and Its Biological Applications. *ACS Nano* **2019**, *13*, 4876–4882.
(27) Po, H. N.; Senozan, N. M. The Henderson–Hasselbalch Equation: Its History and Limitations. *J. Chem. Educ.* **2001**, *78*, 1499–1503.
(28) Debye, P.; Hückel, E. The Theory of Electrolytes. I. Freezing Point Depression and Related Phenomena. *Phys. Z.* **1923**, *24*, 185–206.
(29) Roy, S.; Zhu, D.; Parak, W. J.; Feliu, N. Lysosomal Proton Buffering of Poly(ethylenimine) Measured In Situ by Fluorescent pH-Sensor Microcapsules. *ACS Nano* **2020**, *14*, 8012–8023.
(30) Singh, B.; Maharjan, S.; Park, T.-E.; Jiang, T.; Kang, S.-K.; Choi, Y.-J.; Cho, C.-S. Tuning the Buffering Capacity of Polyethylenimine with Glycerol Molecules for Efficient Gene Delivery: Staying In or Out of the Endosomes. *Macromol. Biosci.* **2015**, *15*, 622–635.
(31) Hanif, M.; Abbas, G. pH-Responsive Alginate-Pectin Polymeric Rafts and Their Characterization. *Adv. Polym. Technol.* **2018**, *37*, 1496–1506.
(32) Shen, J.-Q.; Liao, P.-Q.; Zhou, D.-D.; He, C.-T.; Wu, J.-X.; Zhang, W.-X.; Zhang, J.-P.; Chen, X.-M. Modular and Stepwise Synthesis of a Hybrid Metal–Organic Framework for Efficient Electrocatalytic Oxygen Evolution. *J. Am. Chem. Soc.* **2017**, *139*, 1778–1781.
(33) Feng, L.; Wang, K.-Y.; Willman, J.; Zhou, H.-C. Hierarchy in Metal–Organic Frameworks. *ACS Centr. Sci.* **2020**, *6*, 359–367.
(34) Song, Z.; Wu, Y.; Cao, Q.; Wang, H.; Wang, X.; Han, H. pH-Responsive, Light-Triggered on-Demand Antibiotic Release from Functional Metal–Organic Framework for Bacterial Infection Combination Therapy. *Adv. Funct. Mater.* **2018**, *28*, 1800011.
(35) Sun, Q.; Bi, H.; Wang, Z.; Li, C.; Wang, X.; Xu, J.; Zhu, H.; Zhao, R.; He, F.; Gai, S.; Yang, P. Hyaluronic Acid-Targeted and pH-Responsive Drug Delivery System Based on Metal–Organic Frameworks for Efficient Antitumor Therapy. *Biomaterials* **2019**, *223*, 119473.
(36) Guo, J.; Ping, Y.; Ejima, H.; Alt, K.; Meissner, M.; Richardson, J. J.; Yan, Y.; Peter, K.; von Elverfeldt, D.; Hagemeyer, C. E.; Caruso, F. Engineering Multifunctional Capsules through the Assembly of Metal–Phenolic Networks. *Angew. Chem. Int. Ed.* **2014**, *53*, 5546–5551.
(37) Rahim, M. A.; Kristufek, S. L.; Pan, S.; Richardson, J. J.; Caruso, F. Phenolic Building Blocks for the Assembly of Functional Materials. *Angew. Chem. Int. Ed.* **2019**, *58*, 1904–1927.
(38) Li, K.; Dai, Y.; Chen, W.; Yu, K.; Xiao, G.; Richardson, J. J.; Huang, W.; Guo, J.; Liao, X.; Shi, B. Self-Assembled Metal–Phenolic Nanoparticles for Enhanced Synergistic Combination Therapy against Colon Cancer. *Adv. Biosyst.* **2019**, *3*, 1800241.
(39) Ju, Y.; Cui, J.; Mullner, M.; Suma, T.; Hu, M.; Caruso, F. Engineering Low-Fouling and pH-Degradable Capsules through the Assembly of Metal–Phenolic Networks. *Biomacromolecules* **2015**, *16*, 807–814.
(40) Kim, B. J.; Han, S.; Lee, K. B.; Choi, I. S. Biphasic Supramolecular Self-Assembly of Ferric Ions and Tannic Acid across Interfaces for Nanofilm Formation. *Adv. Mater.* **2017**, *29*, 1700784.
(41) Besford, Q. A.; Ju, Y.; Wang, T. Y.; Yun, G.; Cherepanov, P.; Hagemeyer, C. E.; Cavalieri, F.; Caruso, F. Self-Assembled Metal–Phenolic Networks on Emulsions as Low-Fouling and pH-Responsive Particles. *Small* **2018**, *14*, e1802342.
(42) Ping, Y.; Guo, J.; Ejima, H.; Chen, X.; Richardson, J. J.; Sun, H.; Caruso, F. pH-Responsive Capsules Engineered from Metal–Phenolic Networks for Anticancer Drug Delivery. *Small* **2015**, *11*, 2032–2036.
(43) Ju, Y.; Cortez-Jugo, C.; Chen, J.; Wang, T. Y.; Mitchell, A. J.; Tsantikos, E.; Bertleff-Zieschang, N.; Lin, Y. W.; Song, J.; Cheng, Y.; Mettu, S.; Rahim, M. A.; Pan, S.; Yun, G.; Hibbs, M. L.; Yeo, L. Y.; Hagemeyer, C. E.; Caruso, F. Engineering of Nebulized Metal–Phenolic Capsules for Controlled Pulmonary Deposition. *Adv. Sci.* **2020**, *7*, 1902650.
(44) Dai, Y.; Yang, Z.; Cheng, S.; Wang, Z.; Zhang, R.; Zhu, G.; Wang, Z.; Yung, B. C.; Tian, R.; Jacobson, O.; Xu, C.; Ni, Q.; Song, J.; Sun, X.; Niu, G.; Chen, X. Toxic Reactive Oxygen Species Enhanced Synergistic Combination Therapy by Self-Assembled Metal–Phenolic Network Nanoparticles. *Adv. Mater.* **2018**, *30*, 1704877.
(45) Liang, H.; Li, J.; He, Y.; Xu, W.; Liu, S.; Li, Y.; Chen, Y.; Li, B. Engineering Multifunctional Films Based on Metal–Phenolic Networks for Rational pH-Responsive Delivery and Cell Imaging. *ACS Biomater. Sci. Eng.* **2016**, *2*, 317–325.
(46) Chen, J.; Li, J.; Zhou, J.; Lin, Z.; Cavalieri, F.; Czuba-Wojnilowicz, E.; Hu, Y.; Glab, A.; Ju, Y.; Richardson, J. J.; Caruso, F. Metal–Phenolic Coatings as a Platform to Trigger Endosomal Escape of Nanoparticles. *ACS Nano* **2019**, *13*, 11653–11664.
(47) Xiong, L.; Bi, J.; Tang, Y.; Qiao, S. Z. Magnetic Core–Shell Silica Nanoparticles with Large Radial Mesopores for siRNA Delivery. *Small* **2016**, *12*, 4735–4742.
(48) Zhou, J.; Lin, Z.; Ju, Y.; Rahim, M. A.; Richardson, J. J.; Caruso, F. Polyphenol-Mediated Assembly for Particle Engineering. *Acc. Chem. Res.* **2020**, *53*, 1269–1278.
(49) Zhang, Y.; Wang, Q.; Hess, H. Increasing Enzyme Cascade Throughput by pH-Engineering the Microenvironment of Individual Enzymes. *ACS Catal.* **2017**, *7*, 2047–2051.
(50) Urbansky, E. T.; Schock, M. R. Understanding, Deriving, and Computing Buffer Capacity. *J. Chem. Educ.* **2000**, *77*, 1640–1644.
(51) Zhang, L.; Liu, R.; Gung, B. W.; Tindall, S.; Gonzalez, J. M.; Halvorson, J. J.; Hagerman, A. E. Polyphenol–Aluminum Complex Formation: Implications for Aluminum Tolerance in Plants. *J. Agric. Food Chem.* **2016**, *64*, 3025–3033.
(52) Ottosson, N.; Wernersson, E.; Soderstrom, J.; Pokapanich, W.; Kaufmann, S.; Svensson, S.; Persson, I.; Ohrwall, G.; Bjorneholm, O. The Protonation State of Small Carboxylic Acids at the Water Surface from Photoelectron Spectroscopy. *Phys. Chem. Chem. Phys.* **2011**, *13*, 12261–12267.
(53) Ottosson, N.; Romanova, A. O.; Soderstrom, J.; Bjorneholm, O.; Ohrwall, G.; Fedorov, M. V. Molecular Sinkers: X-Ray Photoemission and Atomistic Simulations of Benzoic Acid and Benzoate at the Aqueous Solution/Vapor Interface. *J. Phys. Chem. B* **2012**, *116*, 13017–13023.
(54) Pan, S.; Guo, R.; Bertleff-Zieschang, N.; Li, S.; Besford, Q. A.; Zhong, Q. Z.; Yun, G.; Zhang, Y.; Cavalieri, F.; Ju, Y.; Goudeli, E.; Richardson, J. J.; Caruso, F. Modular Assembly of Host–Guest Metal–Phenolic Networks Using Macrocyclic Building Blocks. *Angew. Chem. Int. Ed.* **2020**, *59*, 275–280.
(55) Zhong, Q. Z.; Li, S.; Chen, J.; Xie, K.; Pan, S.; Richardson, J. J.; Caruso, F. Oxidation-Mediated Kinetic Strategies for Engineering Metal–Phenolic Networks. *Angew. Chem. Int. Ed.* **2019**, *58*, 12563–12568.
(56) Ma, Y.; Sun, J.; Shen, J. Ion-Triggered Exfoliation of Layer-by-Layer Assembled Poly(acrylic acid)/Poly(allylamine hydrochloride) Films from Substrates: A Facile Way to Prepare

Free-Standing Multilayer Films. *Chem. Mater.* **2007**, *19*, 5058–5062.
(57) Guo, Y.; Geng, W.; Sun, J. Layer-by-Layer Deposition of Polyelectrolyte–Polyelectrolyte Complexes for Multilayer Film Fabrication. *Langmuir* **2009**, *25*, 1004–1010.
(58) Rahim, M. A.; Kempe, K.; Müllner, M.; Ejima, H.; Ju, Y.; van Koeverden, M. P.; Suma, T.; Braunger, J. A.; Leeming, M. G.; Abrahams, B. F.; Caruso, F. Surface-Confined Amorphous Films from Metal-Coordinated Simple Phenolic Ligands. *Chem. Mater.* **2015**, *27*, 5825–5832.
(59) Cupic, K. I.; Rennick, J. J.; Johnston, A. P.; Such, G. K. Controlling Endosomal Escape Using Nanoparticle Composition: Current Progress and Future Perspectives. *Nanomedicine* **2019**, *14*, 215–223.
(60) Seidel, R.; Pohl, M. N.; Ali, H.; Winter, B.; Aziz, E. F. Advances in Liquid Phase Soft-X-Ray Photoemission Spectroscopy: A New Experimental Setup at BESSY II. *Rev. Sci. Instrum.* **2017**, *88*, 073107.
(61) Seidel, R.; Winter, B.; Bradforth, S. E. Valence Electronic Structure of Aqueous Solutions: Insights from Photoelectron Spectroscopy. *Annu. Rev. Phys. Chem.* **2016**, *67*, 283–305.
(62) Winter, B.; Faubel, M. Photoemission from Liquid Aqueous Solutions. *Chem. Rev.* **2006**, *106*, 1176–1211.
(63) Faria, M.; Bjornmalm, M.; Thurecht, K. J.; Kent, S. J.; Parton, R. G.; Kavallaris, M.; Johnston, A. P. R.; Gooding, J. J.; Corrie, S. R.; Boyd, B. J.; Thordarson, P.; Whittaker, A. K.; Stevens, M. M.; Prestidge, C. A.; Porter, C. J. H.; Parak, W. J.; Davis, T. P.; Crampin, E. J.; Caruso, F. Minimum Information Reporting in Bio-Nano Experimental Literature. *Nat. Nanotechnol.* **2018**, *13*, 777–785.

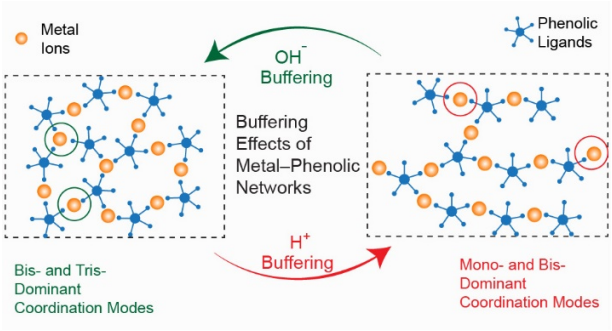

Insert Table of Contents artwork here